Materials Science & Engineering A 894 (2024) 146175

Contents lists available at ScienceDirect

Materials Science & Engineering A

journal homepage: www.elsevier.com/locate/msea

# Experimental and numerical study on hydrogen-induced failure of X65 pipeline steel

Meichao Lin [a], Haiyang Yu [b,**], Dong Wang [c], Andrés Díaz [d], Antonio Alvaro [e], Vigdis Olden [e], Erik Koren [c], Yu Ding [a], Jianying He [a], Zhiliang Zhang [a,*]

[a] Department of Structural Engineering, Norwegian University of Science and Technology (NTNU), Trondheim, 7491, Norway
[b] Division of Applied Mechanics, Department of Materials Science and Engineering, Uppsala University, SE-75121, Uppsala, Sweden
[c] Department of Mechanical and Industrial Engineering, Norwegian University of Science and Technology (NTNU), Trondheim, 7491, Norway
[d] University of Burgos, Escuela Politécnica Superior, Avenida Cantabria S/n, Burgos, 09006, Spain
[e] SINTEF Industry, Trondheim, 7456, Norway

ARTICLE INFO

*Keywords:*
Hydrogen embrittlement
Pipeline steel
Failure criterion
Complete Gurson model

ABSTRACT

Hydrogen-induced fracture of X65 pipeline steel under in-situ electrochemical charging is investigated by using slow strain-rate tensile (SSRT) test, hydrogen diffusion test, fractography analysis, and finite element simulation. Smooth and notched tensile specimens with varying notch radii are utilized to ascertain the impact of stress triaxiality on hydrogen embrittlement (HE) susceptibility. A fully coupled model, H-CGM$^{+}$, capable of simulating the synergy between hydrogen-enhanced plasticity and decohesion, is employed. The simulation proficiently replicates both the global stress-strain trajectories and the local failure initiation sites of the in-situ SSRT tests. The findings indicate a predominance of dislocation trapping hydrogen mechanism in HE, with crack inception at the notch surface where local plastic strain peaks, subsequently advancing towards the center of the specimen. Notably, an inverse relationship is observed between HE susceptibility and stress triaxiality. A hydrogen-induced failure criterion, defined as a critical combination of local hydrogen concentration and plastic strain, is derived. The failure criterion is found to be independent of stress triaxiality, which serves as a good reference for safety assessment of hydrogen pipelines.

## 1. Introduction

Hydrogen as a green energy carrier is believed to be one of the key players in the transition from fossil fuels to renewable energy. Pipelines are a crucial infrastructure for hydrogen gas transport. Yet, pipeline steels are vulnerable to mechanical degradation and premature failure upon exposure to hydrogen, a phenomenon recognized as hydrogen embrittlement (HE) [1]. This poses a critical threat to the structural integrity of pipelines. Comprehending and forecasting the influence of hydrogen on the mechanical properties of pipeline steels is critical for the secure transport of hydrogen.

Extensive research over the past decades has revealed the impact of various factors on HE in pipeline steels. Studies have shown that the type, content, and morphology of inclusions [2–5], along with alloying elements [6,7] and microstructures [8–10], significantly affect HE susceptibility. Various loading conditions such as tensile tests [9,11,12], fatigue tests [13,14], and nanoindentation tests [15] have been employed to understand HE behavior across different scales. The effects of hydrogen under electrochemical [11,16] and high-pressure gaseous charging [8,9] have been examined and compared [12,17,18]. Gaseous charging is more relevant for hydrogen pipelines, while electrochemical charging is preferred for its efficiency, cost-effectiveness, and fewer regulatory hurdles, remaining crucial for routine or preliminary testing in pipeline applications. A recent study proposed an equivalence relation between these charging methods [19], reinforcing the relevance of electrochemical charging for hydrogen pipelines. Despite hydrogen's universally negative impact on the mechanical properties of pipeline steels, its effects and the HE behavior vary significantly, necessitating focused attention on specific conditions.

Pipeline steels respond differently under distinct hydrogen charging conditions [12,18]. Ex-situ charging, where hydrogen is introduced before applying mechanical stress, tends to have a lesser impact

* Corresponding author.
** Corresponding author.
*E-mail addresses:* haiyang.yu@angstrom.uu.se (H. Yu), zhiliang.zhang@ntnu.no (Z. Zhang).

https://doi.org/10.1016/j.msea.2024.146175
Received 17 November 2023; Received in revised form 8 January 2024; Accepted 25 January 2024
Available online 1 February 2024

compared to in-situ charging, where steel is simultaneously exposed to hydrogen and mechanical stress. Research by Wang et al. [12] demonstrated negligible effects of ex-situ charging on X65 pipeline steel, while in-situ charging led to considerable degradation. For X70 pipeline steel, Wang [18] found that fracture toughness decreased with increasing hydrogen levels due to the HELP mechanism [20] during ex-situ charging. In contrast, the fracture toughness decreased linearly with the logarithm of hydrogen concentration when the same material was tested under in-situ hydrogen charging condition and the hydrogen enhanced decohesion (HEDE) mechanism [21] was dominant. Moreover, stress triaxiality may play an important role in hydrogen-induced fracture. A recent study by Depraetere et al. [22] examined the effect of stress triaxiality on HE behavior in a X70 pipeline steel using the ex-situ method. They found that HE susceptibility increased with the increase of stress triaxiality, which was attributed to a greater effect of hydrogen-enhanced lateral void growth, associated with the HELP mechanism. However, the role of stress triaxiality under in-situ conditions is not fully understood, highlighting an area for further investigation.

A notable gap in HE research is the absence of a definitive hydrogen-induced failure criterion. HE initiates locally due to a specific combination of stress, strain, and hydrogen concentration in the material [23,24]. This critical combination at the failure initiation can therefore serve as a potential hydrogen-induced failure criterion. While microscale tests can identify crack nucleation sites [15,17] and hydrogen-rich areas [25], measuring localized stress, strain, and hydrogen concentration directly is challenging. Continuum-scale models, such as the hydrogen informed cohesive zone model [26,27] and the hydrogen informed complete Gurson model [28,29], facilitate the exploration of these parameters at failure initiation points. Establishing an accurate HE criterion requires a synergistic approach combining both experimental observations and numerical simulations to capture the complex nature of HE.

Continuum-scale HE simulations have evolved significantly, incorporating various factors affecting HE. The diffusion coupled cohesive zone model (H-CZM) is one such approach, accounting for hydrogen redistribution [26,27], surface kinetics [30], cyclic loading [31,32] and three-dimensional problems [33,34]. H-CZM primarily addresses the HEDE mechanism. On the other hand, the hydrogen informed complete Gurson model (H-CGM) [28,29] and unit cell analysis [35,36] focus on plasticity-mediated mechanisms, particularly HELP. Recently, Depraetere et al. [37] augmented the H-CGM model with an improved expression for hydrogen-promoted void nucleation in line with the HESIV mechanism [38]. Despite their effectiveness, these models [28,29,37] typically focus on hydrogen-enhanced plasticity with less consideration on decohesion, while the two mechanisms often simultaneously contribute to HE in metals [18,39–45]. In reality, HELP may dominate at low hydrogen concentrations while HEDE dominates at high hydrogen concentrations [39,40,43]. To overcome these limitations, a new unified model, H-CGM$^+$ [46], was proposed, integrating both HELP and HEDE mechanisms. H-CGM$^+$ effectively simulates the competitive dynamics between ductile, HELP, and HEDE mechanisms, and accurately represents the transition of fracture surface morphology seen in various hydrogen conditions. It is noted that another version was recently proposed by Lopes Pinto et al. [47] based on a modified GTN model with consideration of the HEDE mechanism.

In this study, a combination of experimental and numerical methods is employed to elucidate the HE mechanism of X65 pipeline steel under in-situ charging conditions and to establish a hydrogen-induced failure criterion. The investigation assesses the impact of stress triaxiality by analyzing specimens with different notch configurations. Mechanical properties are gauged using slow strain-rate tensile tests (SSRT) performed in air, complemented by hydrogen diffusion and trapping data obtained from parallel studies. The H-CGM$^+$ model is utilized to simulate the loading curves of in-situ SSRT tests, and the fracture surfaces are examined to identify the fracture mechanism. Eventually, the H-CGM$^+$ model enables the determination of the critical combination of localized strain and hydrogen concentration that triggers crack initiation.

## 2. Experimental study

The studied material is a commercial X65 grade carbon steel with a relatively homogeneous microstructure (ferrite matrix and bainite) [12], the mechanical behavior is assumed to be isotropic. Axisymmetric tensile specimens with different geometries, denoted as Smooth, U, M and V are machined according to the dimensions given in Fig. 1. The initial stress triaxiality at the center is calculated using Bridgman's formula [48] as 0.33, 0.8, 1.05 and 1.25 for Smooth, U, M and V, respectively. Note that the triaxiality levels will vary upon the development of plasticity. SSRT tests in air and under in-situ hydrogen charging condition are performed at room temperature. Prior to the tensile testing and hydrogen charging, the sample surface is mechanically ground till 5000 grit SiC paper followed by fine polishing processes. For each geometry, the specimens are tensile tested at a fixed displacement rate. This rate is adjusted for each geometry, such that the local strain rate at the notch root in each specimen is equal to $1 \times 10^{-6}/s$. The variation of the minimum cross-sectional radius is monitored using two perpendicularly positioned cameras. Hydrogen is introduced into the sample by electrochemical charging in an aqueous solution of 3.5 wt% NaCl at a charging potential of $-1050\ mV_{Ag/AgCl}$. Before in-situ SSRT testing, the specimen is pre-charged for 24 h. Fracture surfaces after SSRT test are examined using scanning electron microscope (SEM).

To determine the hydrogen uptake into the sample after pre-charged, hot extraction test is conducted at 600 °C, and the estimated hydrogen concentration is about 0.052 wppm. In a parallel research on the same material: it is determined that the effective hydrogen diffusivity $D_{eff}$ is $2.3 \times 10^{-4}\ mm^2/s$; based on such values it is estimated that a 24 h pre-charging stage would guarantee a uniform hydrogen distribution through the specimen; it is also confirmed that dislocation is the main type of hydrogen trapping site, the corresponding trap binding energy $E_b = 23.0\ kJ/mol$, and the trap density $N_T$ without plastic deformation is $9.09 \times 10^{24}\ site/m^3$. These results are determined by means of permeation test and thermal desorption analysis (TDA), which will be reported in a separate publication.

## 3. Numerical method

Numerical simulation of the SSRT tests in air and in hydrogen charging condition is carried out in ABAQUS, and the finite element model considers only half of the tensile specimen due to symmetry. An example (M-notch specimen) is shown in Fig. 2(a), the same loading displacement rate as used in the SSRT test is applied to the top nodes, while the bottom nodes are pinned. The mesh consists of 9252 elements with a minimum mesh size of 0.1 *mm*.

### 3.1. Numerical simulations without hydrogen

An extended complete Gurson model (CGM), CGM$^+$ [46] implemented through a VUMAT subroutine in ABAQUS, is used for simulations without hydrogen. The complete Gurson model (CGM) [49] is designed to model ductile failure by a voiding process where both the homogeneous and the localized deformation of voids are represented. CGM$^+$ is obtained by integrating a stress-controlled decohesion criterion into CGM. The schematic of CGM$^+$ is shown in Fig. 2(b). Path A illustrates the classical GTN model [50], where the homogeneous deformation of void (i.e. void growth) is represented, the term $\sigma_1$ is the applied maximum principal stress. Path B illustrates the Thomason's plastic limit load model [51], where the localized deformation of void (void coalescence) is represented, the term $\sigma_1^{localized}$ is the threshold stress for localized deformation mode. Path A is favorable when the equivalent

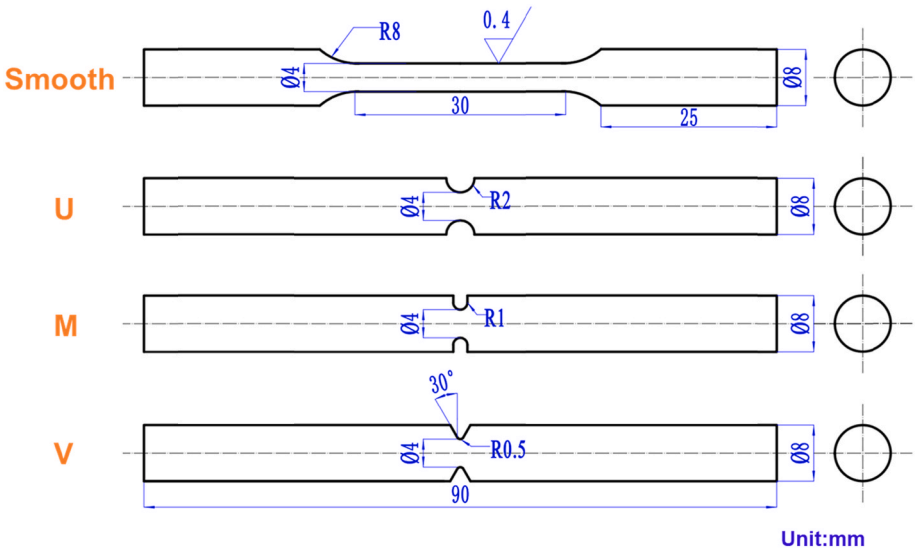


**Fig. 1.** The dimensions of Smooth, U, M and V tensile specimens. The surface roughness after machining is 0.4.

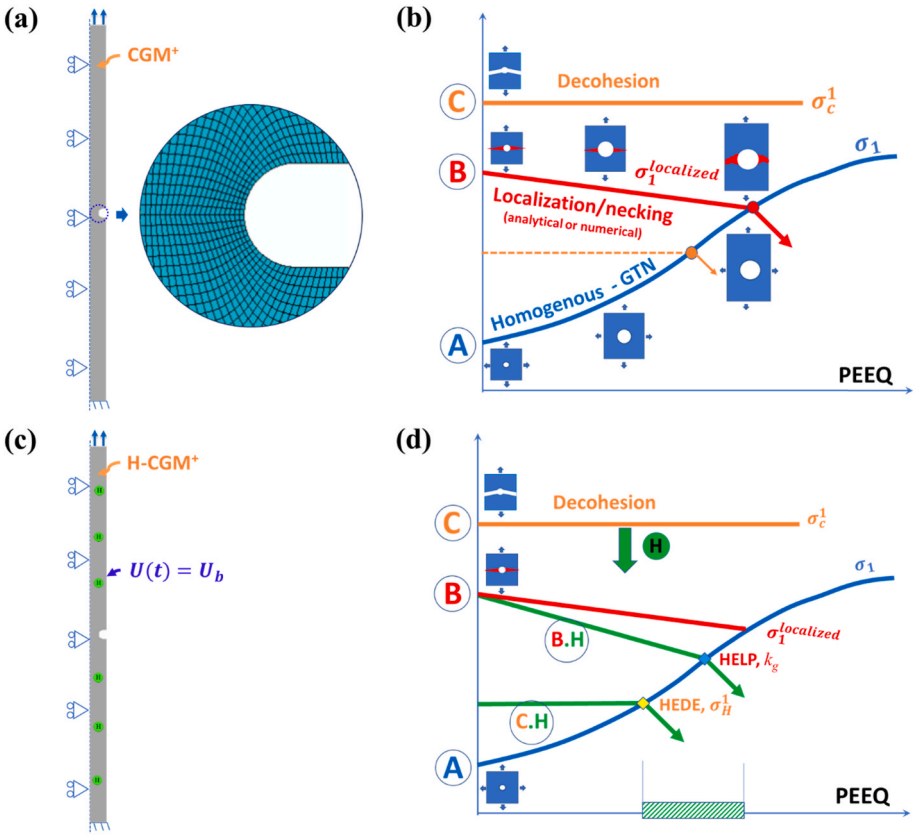


**Fig. 2.** (a) Finite element model of the M-notch specimen and the distribution of mesh close to the notch; (b) The schematic of $CGM^+$, showing the coexistence of void coalescence and decohesion criteria; (c) Boundary conditions used in the simulations with hydrogen, $U(t) = U_b$ means the chemical potential at the boundary is constant during in-situ SSRT test; (d) The schematic of $H\text{-}CGM^+$, showing the competition between HELP and HEDE.

plastic strain (PEEQ) is small since the stress required for void growth is smaller than that for void coalescence, until it intersects with path B, as indicated by the red dot in Fig. 2(b), then void coalescence becomes favorable. Path A and path B represent the CGM where the void coalescence is automatically predicted and the void volume fraction at intersecting point indicates the critical void volume fraction $f_c$. Path C shows the stress-based decohesion criterion, the term $\sigma_c^1$ is the decohesion threshold/cohesive strength. The actual failure mode of $CGM^+$ depends on the competition between void coalescence and decohesion. When $\sigma_c^1$ is sufficiently large (orange solid line), void coalescence prevails, $CGM^+$ returns to CGM, and failure occurs at the red dot. If $\sigma_c^1$ is small (orange dash line), decohesion takes charge, and $CGM^+$ fails at the orange dot. Considering that all the samples exhibit ductile fracture mode with micro-void coalescence features when hydrogen is absent, as proved by SEM observation, $\sigma_c^1$ is assumed to be high, so that void

coalescence controls failure.

$$\textbf{\textit{Path A}}: \varnothing(\boldsymbol{\sigma}, \overline{\sigma}, f) = \left(\frac{\sigma_e}{\overline{\sigma}}\right)^2 + 2q_1 f cosh\left(\frac{q_2\sigma_m}{2\overline{\sigma}}\right) - 1 - q_1^2 f^2 = 0 \quad (1)$$

$\sigma_e$ is the conventional von Mises stress, $\overline{\sigma}$ is the flow stress of the matrix material, $\sigma_m$ is the mean stress and $f$ is the current void volume fraction, $q_1$ and $q_2$ are the coefficients introduced by Tvergaard [50].

$$\textbf{\textit{Path B}}: \sigma_1^{localized} = \overline{\sigma}\left(\alpha\left(\frac{1}{r} - 1\right)^2 + \frac{\beta}{\sqrt{r}}\right)\left(1 - \frac{\pi}{4}r^2\right) \quad (2)$$

$r$ is the void space ratio, $\alpha$ and $\beta$ are constants, typically $\alpha = 0.12 + 1.68{*}n$ ($n$ is the hardening exponent) and $\beta = 1.2$ according to Zhang [52].

$$\textbf{\textit{Path C}}: \sigma_c^1 = \sigma_0 \times \gamma \quad (3)$$

$\sigma_0$ is the yield stress of the matrix material, $\gamma$ is the decohesion threshold parameter [46,53].

The application of CGM$^+$/CGM needs determination of several mechanical properties including elastic parameters ($E, \nu$), flow properties ($n$, equivalent $\sigma$-$\varepsilon$ curve), coefficients of yield function ($q_1, q_2$), void nucleation parameters and ductile fracture parameters. The elastic and hardening properties can be directly derived from experimental result. Regarding to the coefficients of yield function, the commonly used values $q_1 = 1.5$ and $q_2 = 1.0$ are chosen [54]. In the current study, void nucleation is represented by the cluster nucleation model [52], where the only controlling parameter is initial void volume fraction $f_0$. By fitting the SSRT testing results with CGM$^+$, the parameter $f_0$ is identified. These mechanical properties are then transferred to simulations with hydrogen.

### 3.2. Numerical simulations with hydrogen

H-CGM$^+$ [46] is used to model the in-situ SSRT results. As a fully coupled model, H-CGM$^+$ incorporates the hydrogen redistribution during loading as well as the mechanical response because of localized hydrogen. This is realized through a VUMAT subroutine combined with a VUMATHT subroutine. The VUMATHT subroutine is coded based on the chemical potential strategy [55], where the lattice chemical potential rather than lattice hydrogen concentration is the variable to solve for. One advantage of this scheme is that we may prescribe a constant lattice chemical potential as boundary condition while modelling the scenarios of a metal exposed to and in equilibrium with a hydrogen atmosphere (i.e. in-situ SSRT) [55,56]. Otherwise stress-dependent lattice concentration type of boundary condition would be needed since the stress state on the boundary will affect the permeation of hydrogen [55,56]. First a uniform lattice hydrogen concentration is assigned across the specimen to mimic the case after 24 h of pre-charging; then the lattice chemical potential at the boundary is set to be constant during loading, to account for hydrogen permeation, as shown in Fig. 2(c).

H-CGM$^+$ is designed to capture the competition/transition between HELP and HEDE, where HELP is modelled through a hydrogen-induced acceleration of the voiding process and HEDE is realized by a degradation of the decohesion threshold. In present study, we assume that the rate of void growth increases linearly with hydrogen concentration to account for HELP, following Yu et al. [28] and Depraetere et al. [29].

$$\dot{f}_{growth}(C) = \dot{f}_{growth0}\left(1 + k_g C\right) \quad (4)$$

$\dot{f}_{growth0}$ is the void growth rate without hydrogen, $C$ is the total hydrogen concentration, $k_g = 0.16$ is the hydrogen assisted degradation factor. This operation ensures that path B has a sharper slope of decrease (B.H), which makes $\sigma_1^{localized}$ intersect earlier with $\sigma_1$, resulting in an earlier failure (at blue diamond), as shown in Fig. 2(d). On the other hand, HEDE is implemented through lowering the decohesion threshold $\sigma_c^1$ to an appropriate value $\sigma_H^1$, path C hence shifts downward (C.H), which also leads to an earlier intersection with $\sigma_1$ (at yellow diamond). The actual failure mechanism depends on the magnitude of degradation on $\sigma_c^1$. When hydrogen degradation on $\sigma_c^1$ is significant ($\sigma_H^1$ is low), the intersection with $\sigma_1$ at the yellow diamond appears earlier, and HEDE prevails; If $\sigma_H^1$ is high enough and the intersection with $\sigma_1$ at the blue diamond comes first, HELP dominates. By fitting the in-situ SSRT testing results, we found that HEDE prevails in all hydrogen cases, and a suitable $\sigma_H^1$ is attained for each geometry. This is also confirmed by SEM result, where cleavage facets are observed in all hydrogen charged samples.

To obtain the hydrogen concentration, diffusion models that consider the chemical potential gradient as the driving force [55,56] and solving the lattice chemical potential as the variable are carried out. Hydrogen might be localized in lattice sites (L subscript) or trapping sites (T subscript):

$$C_L = N_L\theta_L \quad (5)$$

$$C_T = N_T\theta_T \quad (6)$$

$N_L$ and $N_T$ are the number of sites per unit volume (site density), $\theta_L$ and $\theta_T$ are the occupancy fraction. According to Oriani's equilibrium [57] between $\theta_L$ and $\theta_T$:

$$\frac{\theta_T}{1-\theta_T} = \frac{\theta_L}{1-\theta_L}K_T \quad (7)$$

$$K_T = \exp\left(-\frac{E_B}{RT}\right) \quad (8)$$

$K_T$ is the equilibrium constant, $E_B$ is the trap binding energy, $R$ is the gas constant, $T$ is the temperature. In bcc metals, low occupancy $\theta_L \ll 1$ is usually assumed, such that:

$$\frac{\theta_L}{1-\theta_L} \approx \theta_L \quad (9)$$

Considering (5)–(9):

$$C_T = N_T\frac{K_T C_L}{K_T C_L + N_L} \quad (10)$$

For an isothermal analysis ($T = T_0$):

$$\frac{\partial C_T}{\partial t} = \frac{\partial C_T}{\partial C_L}\frac{\partial C_L}{\partial t} + \frac{\partial C_T}{\partial N_T}\frac{\partial N_T}{\partial \varepsilon^p}\frac{\partial \varepsilon^p}{\partial t} \quad (11)$$

Neglecting the hydrogen flux between traps [58,59], the mass balance can be expressed as:

$$\frac{\partial C_L}{\partial t} + \frac{\partial C_T}{\partial t} = -\nabla\cdot\mathbf{J}_L \quad (12)$$

$$\mathbf{J}_L = -D_L\frac{C_L}{RT}\nabla\mu_L \quad (13)$$

$\mathbf{J}_L$ represents the flux of lattice hydrogen, $D_L$ is the lattice diffusivity. $\mu_L$ is the chemical potential of hydrogen in lattice sites which can be expressed as:

$$\mu_L = \mu_L^0 + RTln\left(\frac{C_L}{N_L}\right) - \overline{V}_H\sigma_h \quad (14)$$

$\mu_L^0$ is the chemical potential in the standard state, $\overline{V}_H$ is the partial molar volume of hydrogen, $\sigma_h$ is the hydrostatic stress. According to the chemical potential strategy proposed by Di Leo and Anand [55], the governing equation is expressed as:

$$\frac{D_L}{D_{eff}}\frac{C_L}{RT_0}\frac{\partial \mu_L}{\partial t} - \nabla\cdot\left(D_L\frac{C_L}{RT_0}\nabla\mu_L\right) + \frac{D_L}{D_{eff}}\frac{C_L}{RT_0}\overline{V}_H\frac{\partial \sigma_h}{\partial t} + \theta_T\frac{dN_T}{d\varepsilon^p}\frac{\partial \varepsilon^p}{\partial t} = 0 \quad (15)$$

In the VUMATHT subroutine, the variation of $u_L$ is solved in each time increment, such that the variation of $C_L$ is obtained accordingly. Based on Oriani's equilibrium [57] in Eq. (10), $C_T$ can be calculated with

the trap binding energy $E_B$ and trap density $N_T$.

For the studied X65 pipeline steel, dislocation is the main trapping type with $E_B = 23.0\ kJ/mol$, and the trap density $N_T$ without plastic deformation ($\varepsilon^p = 0$) is $9.09 \times 10^{24}\ site/m^3$. The dislocation trap density $N_T$ is a function of plastic strain $\varepsilon^p$, and a widely used relation (Eq. (16)) is available for steels. It is revealed that dislocation trap density may have different initial values at $\varepsilon^p = 0$ for different steels, but their evolution with varying $\varepsilon^p$ is identical, as summarized in Fig. 3 [27,60–64].

$$log\ N_T = A - 2.33\ \exp(-5.5\varepsilon_p) \tag{16}$$

A corresponds to the trap density at $\varepsilon^p = 0$. Based on Eq. (16), the value $A = 27.29$ is calculated for the X65 pipeline steel. For comparison, the resulting $N_T$ vs $\varepsilon^p$ plot (red line) is presented in Fig. 3 and it is within the range reported in the literature, indicating a reasonable presumption. Note that the exact values of $N_T$ during deformation are not necessarily consistent with this law, so the localized value of $C_T$ may differ in real situation. To acquire accurate relation between $N_T$ and $\varepsilon^p$, hydrogen permeation test on samples with different levels of pre-strain can be conducted [65].

## 4. Results and discussion

### 4.1. SSRT testing results

Fig. 4(a) shows the experimental engineering stress vs true strain curves ($\sigma_e$-$\varepsilon$) for Smooth, U, M and V samples in air and in the presence of hydrogen. Assuming the studied pipeline behaves in an isotropic manner, the true strain is calculated as $\varepsilon = 2 \times \ln(a_0/a)$, with $a_0$ and $a$ being the initial and the instantaneous minimum cross-sectional radius under loading, respectively. The failure strain is defined as the strain corresponding to the apparent sudden drop of engineering stress. The reason for plotting engineering stress vs true strain curves, rather than engineering stress vs engineering strain curves, is that true strain is independent of the initial specimen length [66]. With the increase of stress triaxiality (i.e. increasing sharpness of the notch), the notch tensile strength increases, while the failure strain decreases. Hydrogen decreases the failure strain but has negligible effect on the notch tensile strength. Similar phenomena were observed in other pipeline steels [18,67]. The strain corresponding to the maximum engineering stress is about 0.1 (grey dash line), indicating that material's hardening exponent $n$ is around 0.1 [68,69].

The HE indexes [70], calculated as $(\varepsilon_{f,air} - \varepsilon_{f,H})/\varepsilon_{f,air}$ for each geometry are plotted in Fig. 4(b), where $\varepsilon_{f,air}$ and $\varepsilon_{f,H}$ are the failure strain in air and in the presence of hydrogen respectively. HE susceptibility decreases with stress triaxiality. This trend is contrary to the result reported in Ref. [22], where X70 pipeline steel was investigated and ex-situ pre-charging method was adopted; the qualitative explanation [22] was that crack initiated at the center, the stress-assisted diffusion caused a higher hydrogen concentration at the center for a larger triaxiality, leading to a larger effect of hydrogen enhanced lateral void growth (HELP) and thus a more embrittlement behavior. As discussed later, the trend in this experiment is also reasonable in light of the in-situ testing condition leading to different crack initiation site as well as different dominant fracture mechanism. As a matter of fact, the influence of stress triaxiality on HE susceptibility is dependent on the material, specimen geometry (i.e. stress concentration factor $K_t$) and environmental condition. With ex-situ charging, a higher HE susceptibility was found in X70 pipeline steel [22] and AISI 4135 steel [71] for specimens with a higher notch severity, while opposite trend was found in martensitic steel [72]. Walter et al. [73] and An et al. [74] found that the loss of ductility increased with $K_t$ firstly, reaching a maximum, and then decreased with $K_t$ in low alloy steels [73] and in X80 pipeline steel [74].

Fracture surfaces after SSRT test are examined in SEM. Samples failing in air all displayed a typical cup-and-cone fracture surface with high density of dimples, indicating a ductile fracture mode. An example (M-notch) is shown in Fig. 5(a–c), where two regions are identified, namely the dimpled inner region and the peripheral region with shear lip. These two regions are produced as a result of crack initiation from the center of specimen, and propagation towards the surface in the nature of unstable fracture [75].

Samples failing in the presence of hydrogen all exhibited a mixed mode of fracture. An example (M-notch) is presented in Fig. 5(d–f), three regions with distinct fracture features are recognized: close to the notch root, quasi-cleavage fracture with facets and ridges is observed (Fig. 5(e1)); at the center of specimen, ductile fracture is observed with large number of dimples (Fig. 5(e3)); there exists a transition area between the notch root and the center characterized by both facets (green arrows) and dimples (yellow arrows) (Fig. 5(e2)). In addition, cracks are observed on the surfaces of the notches, which indicates that failure emanates from the notch surface and then propagates towards the center [8]. This is also confirmed by optical imaging recorded during the tensile test (Fig. 5(f)). The surface-initiated cracking is a prominent feature of hydrogen induced failure in the current study, in contrast to damage initiation from the center without hydrogen. According to the fracture morphology, the HEDE mechanism should be responsible for the fracture under in-situ hydrogen charging. Similar behavior was observed in plain-carbon steels, where fracture surfaces were examined after in-situ SSRT under gaseous hydrogen charging [8]. As discussed later, this may be attributed to the hydrogen distribution which has peak concentration

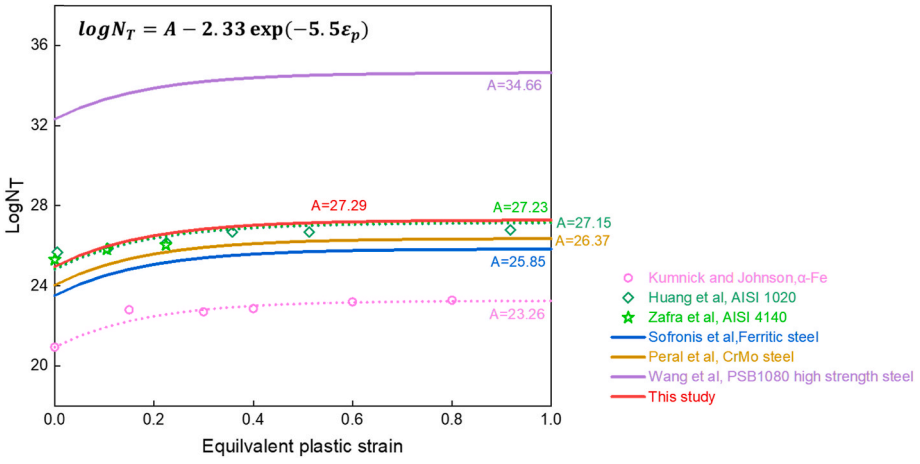


**Fig. 3.** Dislocation trap density $N_T$ as a function of equivalent plastic strain $\varepsilon_p$. Dash lines show fitted curves of experimental data: Kumnick and Johnson [60], Huang et al. [61] and Zafra et al. [62]. Solid lines show analytic laws adopted in literatures: Sofronis et al. [63], Peral et al. [27], and Wang et al. [64].

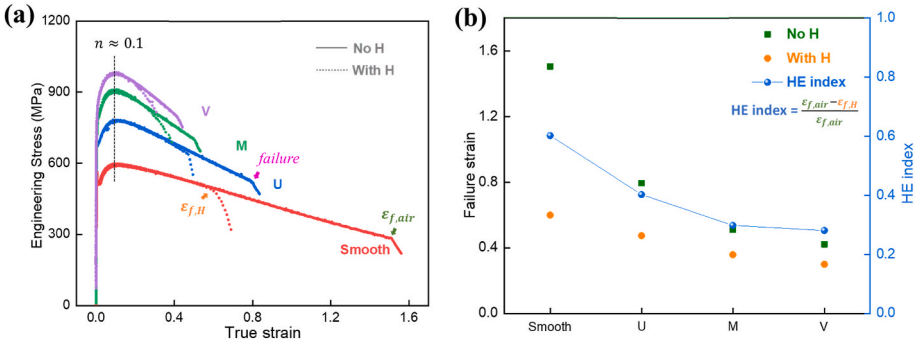


**Fig. 4.** (a) Experimentally obtained engineering stress vs true strain curves ($\sigma_e$-$\varepsilon$) of each geometry in air and in the presence of hydrogen; (b) Failure strain and HE index as a function of geometry.

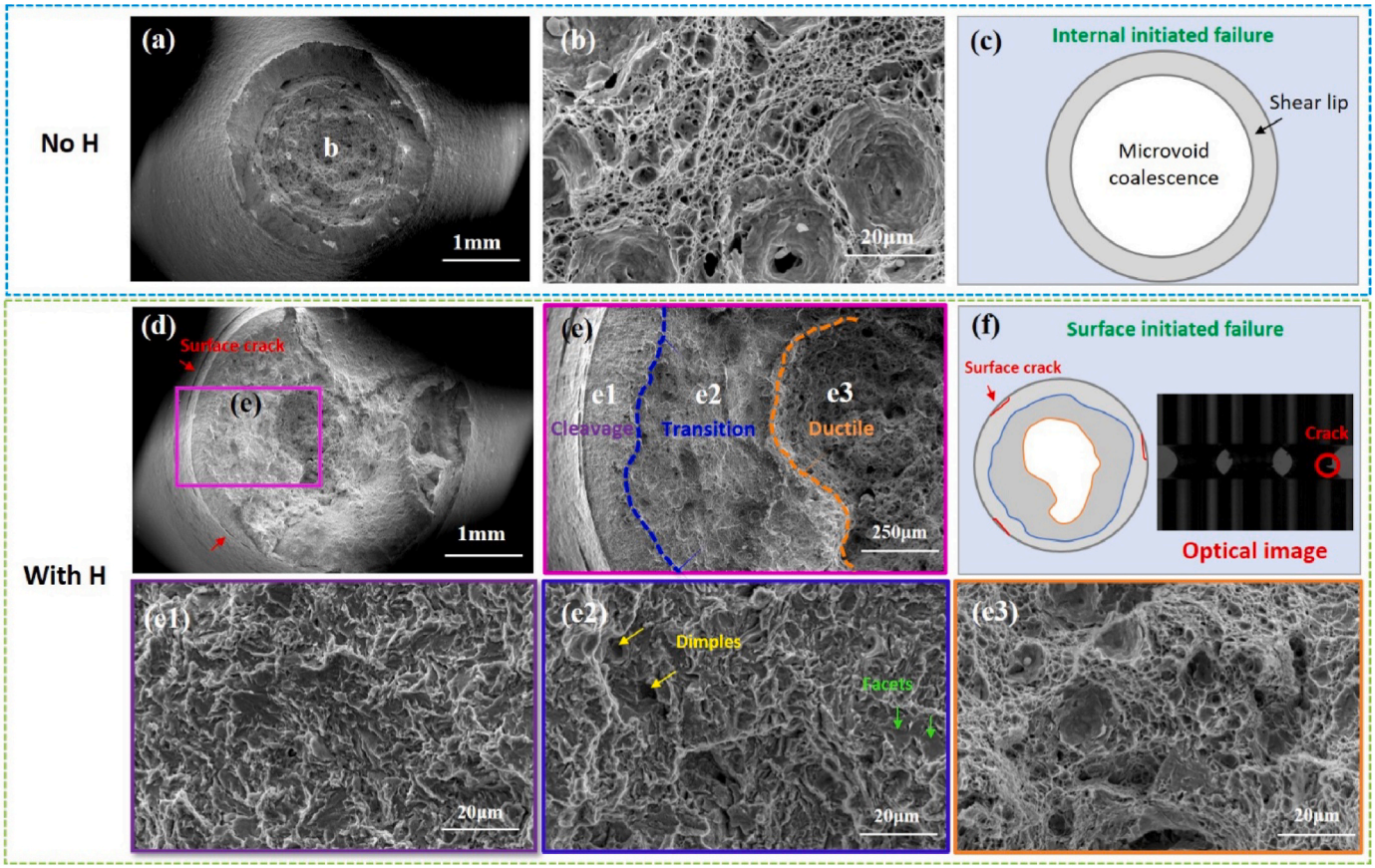


**Fig. 5.** The fracture surfaces of M-notch specimen failed in air (a–c) and in hydrogen charging condition (d–f), indicating the center-initiated ductile fracture and the surface-initiated mix-mode fracture, respectively.

close to the notch root, due to the intensive local plasticity.

### 4.2. Determination of CGM + model parameter

With the loading curves of SSRT tests, it is possible to identify material parameters for the CGM$^+$ model. The main parameters to be calibrated include elasticity, flow properties of the matrix material, and initial void volume fraction $f_0$. Assuming negligible influence of $f_0$ on the flow behavior [76,77], the elasticity and flow properties of the matrix material can be obtained from the stress-strain curve of the M-notch specimen in the absence of hydrogen (Fig. 4(a)). Note that we do not employ the smooth tensile bar, which would need to carry out a Bridgman correction [48] on the tri-axial stress state after necking. With the Bridgman correction, the instantaneous notch radius ratio $a/R$ (the minimum cross section radius $a$ over the notch radius $R$) needs to be monitored during the test. To bypass the challenge, Tu et al. [69,78] designed a tensile bar with the so-called 'magic notch', with which the instantaneous notch radius ratio $a/R$ keeps constant even after necking and $a/R$ can be directly determined from hardening exponent $n$. From the measured true $\sigma$-$\varepsilon$ curve of 'magic notch' (M-notch specimen in Fig. 4(a)), one can easily derive the equivalent stress strain curve without Bridgman correction. The dervied curve, as well as a summary of the elasticity and flow properties, is shown in Fig. 6(a).

Then, a finite element model is built based on the M-notch geometry, as shown in Fig. 2(a) to calibrate $f_0$. The identified elasticity and flow properties are applied. The model is used to simulate the loading curve recorded for the M-notch specimen, by varying $f_0$. After several trial-and-errors, an optimal $f_0$ is identified, 0.00015, as summarized in

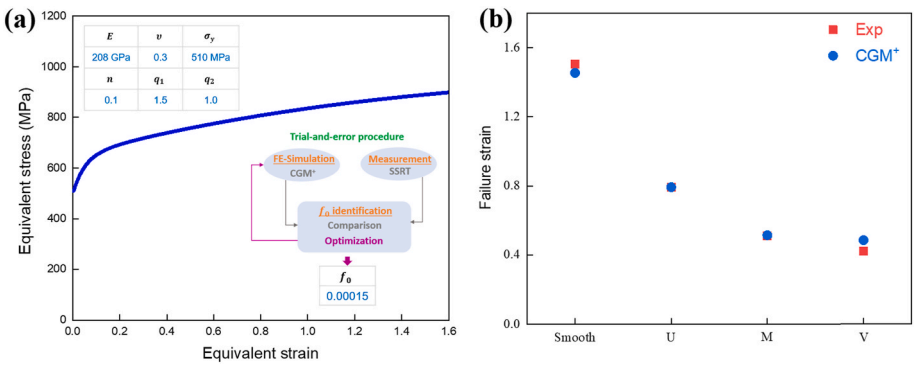


**Fig. 6.** (a) The identified CGM$^+$ parameters for X65 pipeline steel, the inset presents the trial-and-error procedure; (b) Failure strain in the absence of hydrogen, comparison of experiment and simulation (CGM$^+$).

Fig. 6(a).

These CGM$^+$ parameters are geometry independent. To verify, the same set of parameters are applied to simulate the experimental loading curves of Smooth, U-notch and V-notch specimens in Fig. 4(a). As shown in Fig. 7, very good agreement is achieved for each geometry, indicating that the determined parameters are satisfactory. Naturally, the failure loci of all the notched tensile tests are also well captured, as shown in Fig. 6(b).

It is noted that the CGM$^+$ model predicts failure initiation at the center of specimens, consistent with the experimental result without hydrogen (Fig. 5(a–c)). This is because CGM$^+$/CGM adopts the plastic limit load model [51] as the void coalescence/failure criterion. Failure is triggered when the applied maximum principal stress $\sigma_1$ reaches the threshold for localized deformation of void $\sigma_1^{localized}$, as illustrated in Section 3.2. Since $\sigma_1$ reaches its maximum at the center, failure begins there.

### 4.3. Numerical results with hydrogen

Hydrogen diffusion coupled model H-CGM$^+$ is utilized to simulate the loading curves of in-situ SSRT tests. The CGM$^+$ parameters have been calibrated, and hydrogen diffusion and trapping parameters have been measured with permeation test and TDS analysis in a separate study, as summarized in Table 1. To capture hydrogen induced fracture with H-CGM$^+$, one also needs to link the mechanical damage to local hydrogen concentration, i.e., implement an accelerated void growth $k_g$ or establish a hydrogen degradation law. As observed through post-mortem fracture surface investigations (Fig. 5(d–f)) for in-situ hydrogen-charged specimens, the material tearing/cracking process initiates at the notch surface and in the form of hydrogen enhanced

**Table 1**
Hydrogen behavior related parameters [59,79].

| $D_L$ $(mm^2/s)$ | $N_L$ $(site/mm^3)$ | $R$ $(Nmm/molK)$ | $\overline{V}_H$ $(mm^3/mol)$ | $\mu_L^0$ $(kJ/mol)$ |
|---|---|---|---|---|
| $7.387 \times 10^{-3}$ [79] | $5.1 \times 10^{20}$ [59] | $8.314 \times 10^3$ | 2000.0 | 28.6 |
| $T_0$ (K) | $E_b$ $(kJ/mol)$ | $k_g$ | $N_T$ | |
| 300.0 | 23.0 | 0.16 | $\log N_T = 27.29 - 2.33\exp(-5.5\varepsilon_p)$ | |

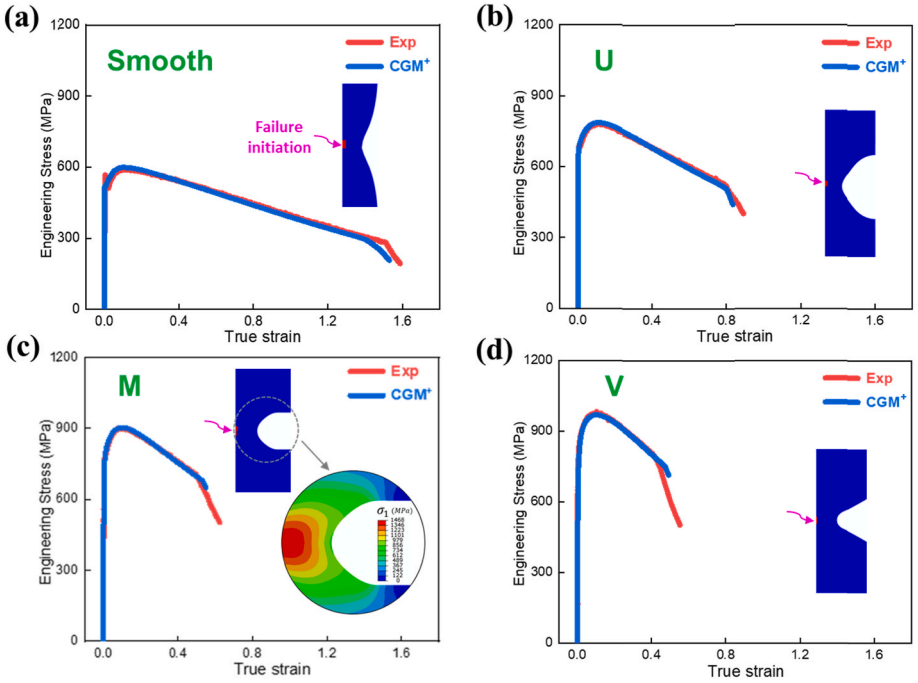


**Fig. 7.** The engineering stress vs true strain curves ($\sigma_e$-$\varepsilon$) in air, comparison of experiment and simulation (CGM$^+$); The insets show failure initiates at the sample center; (c) also gives the distribution of maximum principal stress $\sigma_1$ around the M-notch root at failure.

decohesion. Therefore, establishing a hydrogen degradation law on decohesion threshold $\sigma_H^1$ is essential.

First, the critical failure stress $\sigma_c^1$ at the center of the specimens is extracted from the CGM$^+$ simulation in the absence of hydrogen, i.e., the location of failure for the specimen tested in air. These critical failure stresses are plotted against specimen geometry in Fig. 9(a). H-CGM$^+$ simulations are then performed using an initial hydrogen concentration of 0.052 wppm as measured via hot extraction test before loading. A constant chemical potential is applied at specimen boundaries during loading, to mimic the in-situ charging condition. It is found that the simulated stress strain curves agree well with the experimental curves up to failure. The failure point, however, cannot be readily captured, due to the lack of a hydrogen degradation law. Following the experimental observations, we limit the failure initiation site to the circumference of the specimens and obtained the decohesion threshold $\sigma_H^1$ via trial-and-error method, which gives satisfactory prediction of failure as shown in Fig. 8. These decohesion thresholds $\sigma_H^1$ at the circumference are also plotted against specimen geometry in Fig. 9(a). As can be seen, the critical failure stress increases with the sharpness of the notch, both with and without hydrogen ($\sigma_H^1$ and $\sigma_c^1$), which is in accordance with [71,80,81].

Interestingly, the ratio $k$ between $\sigma_H^1$ and $\sigma_c^1$ is approximately constant, irrespective of the specimen geometry. The ratio $k$ represents the relative degradation of decohesion threshold at a given hydrogen concentration. In a previous study on a high strength steel [80], similar observations was obtained, i.e. the relative hydrogen degradation was independent of the specimen geometry. Such assumption holds as long as the local hydrogen concentrations at the failure sites in the four geometries are similar.

Hydrogen distribution at failure is then investigated, and the concentration contours for the M and V-notched specimens are presented in Fig. 8(c1) and (d1) as examples. At failure, the maximum lattice hydrogen concentration $C_L$ occurs in correspondence of the hydrostatic stress peak, while the trapped hydrogen concentration $C_T$ reaches its maximum at the notch circumference where the local plastic strain is maximum. The maximum total hydrogen concentration $C = C_L + C_T$ occurs at the notch circumference where failure initiates, and the values are 2.8 wppm and 3.1 wppm for the two specimens, respectively. For the U-notched specimen and smooth specimen, the total concentrations at the circumference are 3.0 wppm and 2.6 wppm respectively. Since the local hydrogen concentrations at the failure sites for the four specimens are similar, one should be able to calibrate the hydrogen degradation law on decohesion/stress threshold which are suitable for all the different specimen configurations by using only one geometry (i.e., M-notch). Only one data point on a hydrogen degradation curve is determined through this study. Different current densities or voltages for cathodic charging should be applied to produce varied hydrogen concentrations inside the specimen. Using the H-CGM$^+$ model and following a similar procedure as described earlier, a hydrogen degradation law can then be calibrated.

The local critical concentration is substantially larger than the measured uniform concentration after pre-charging, 0.052 wppm. The reason is that the specimens are loaded under in-situ charging, so that more hydrogen are absorbed due to stress-assisted diffusion and local plasticity. Moreover, trapped hydrogen concentration is significantly higher than lattice concentration, indicating that hydrogen-induced failure is dominated by hydrogen trapping related to dislocation density or local plasticity, given the assumption that both the hydrogen population ($C_L$ *and* $C_T$) contribute equally to the determination of hydrogen degradation of the material. This phenomenon is similar to what was reported in X80 pipeline steel [11]. To further investigate the effect of stress triaxiality on HE susceptibility, the PEEQ values at failure of each geometry are plotted in Fig. 9(b). In absence of hydrogen, the PEEQ value decreases with stress triaxiality, while in the presence of hydrogen, the PEEQ value remains almost constant at around 0.31. The difference between the cases without and with hydrogen can be used as an indicator of HE index, which shows a decreasing trend with stress triaxiality. The fracture mechanism as well as the reason why HE susceptibility decreases with stress triaxiality under in-situ charging condition can be explained as follow: crack initiation occurs when hydrogen concentration reaches a critical value of about 2.8 wppm, and it initiates at the circumference where the local plastic strain is maximum since

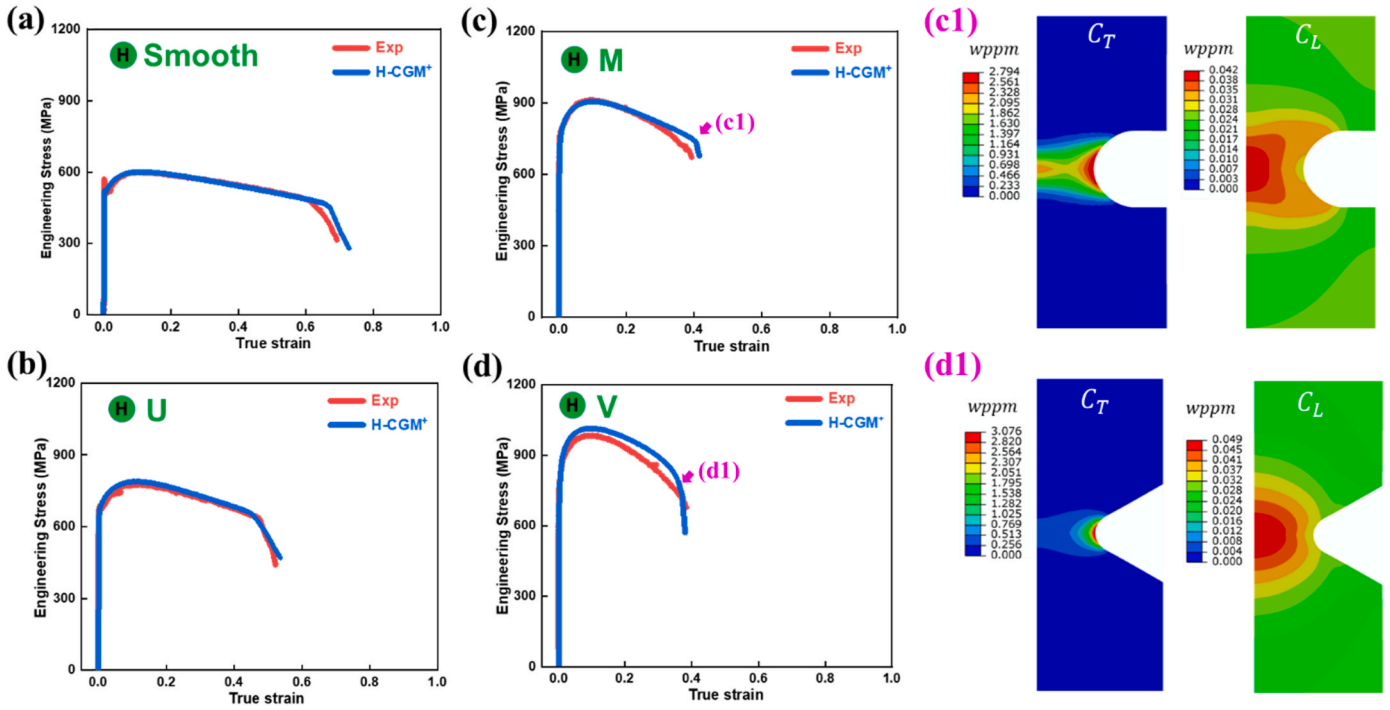


**Fig. 8.** (a–d) The engineering stress vs true strain curves ($\sigma_e$-$\varepsilon$) in the presence of hydrogen, comparison of experiment and simulation (H-CGM$^+$); The distribution of lattice hydrogen concentration $C_L$ and trapped hydrogen concentration $C_T$ at failure for (c1) M-notch and (d1) V-notch specimens.

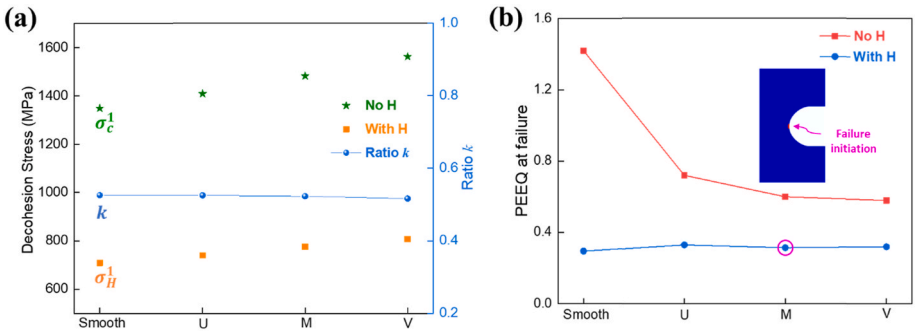


**Fig. 9.** (a) The critical failure stress and the ratio $k = \sigma_H^1/\sigma_c^1$ as a function of geometry; (b) The PEEQ value at failure as a function of geometry. The failure stresses and PEEQ values are local values of the element that fails first: at the center of the specimens (without H) & at the circumference of the specimens (with H).

dislocation trapped hydrogen takes up a major part of total hydrogen. Local equivalent plastic strain at failure remains constant in the presence of hydrogen for all geometries, whereas it has a larger value for the case with lower triaxiality in hydrogen free condition, so that specimens with lower stress triaxiality exhibit more 'embrittlement' behavior. The critical combination of hydrogen concentration and equivalent plastic strain required to trigger crack initiation under in-situ electrochemical charging conditions in X65 pipeline steel is found to be 2.8 wppm and 0.31, respectively; these values are independent of stress triaxiality, can be used as a failure criterion, and are considered as a valuable reference for the safety assessment of hydrogen pipelines.

## 5. Conclusion

The susceptibility of X65 pipeline steel to hydrogen embrittlement under in-situ electrochemical charging is investigated using a combination of experimental and numerical methods. Various notched tensile specimens are employed to examine the role of stress triaxiality on HE. SSRT tests are conducted in air and under hydrogen charging conditions to observe the differences in mechanical behavior. Fracture surfaces from these tests are analyzed to understand the failure mechanisms. Numerically, the H-CGM$^+$ model is utilized to simulate the loading curves and pinpoint local failure initiation sites of the in-situ SSRT tests. This comprehensive approach allows for a detailed assessment of the HE susceptibility of X65 pipeline steel under the specific charging conditions. From the investigation, several conclusions are drawn:

(1) A specific set of mechanical parameters for the X65 pipeline steel has been identified and incorporated into the CGM $^+$ model, as depicted in Fig. 6(a).
(2) Hydrogen is found to slightly affect the notch tensile strength but significantly reduce the failure strain. HE is primarily driven by dislocation trapping hydrogen, with cracks typically initiating at the notch surface where local plastic strain is highest. Interestingly, HE susceptibility decreases as stress triaxiality increases.
(3) The H-CGM$^+$ model effectively replicates both global stress-strain curves and local failure initiation sites from in-situ SSRT tests. The model identifies a critical combination of hydrogen concentration (2.8 wppm) and local strain (0.31) that indicates hydrogen-induced failure. This combination acts as a failure criterion for HE and remains consistent across varying stress triaxialities.

Finally, it should be acknowledged that this failure criterion is specific to certain hydrogen charging conditions. Thus, it might represent just one aspect of a broader hydrogen-induced failure criterion for X65 pipeline steel. To establish a comprehensive failure map, further systematic experimental and modeling efforts under various service conditions are necessary.

## CRediT authorship contribution statement

**Meichao Lin:** Writing – original draft, Visualization, Validation, Methodology, Investigation, Formal analysis, Data curation. **Haiyang Yu:** Writing – review & editing, Validation, Supervision, Software, Methodology, Investigation. **Dong Wang:** Writing – review & editing, Investigation, Data curation. **Andrés Díaz:** Writing – review & editing, Software, Investigation. **Antonio Alvaro:** Writing – review & editing, Supervision, Investigation, Data curation. **Vigdis Olden:** Writing – review & editing, Supervision, Investigation, Funding acquisition. **Erik Koren:** Writing – review & editing, Investigation, Data curation. **Yu Ding:** Writing – review & editing, Investigation. **Jianying He:** Writing – review & editing, Supervision, Project administration, Methodology, Investigation. **Zhiliang Zhang:** Writing – review & editing, Supervision, Project administration, Investigation, Funding acquisition, Conceptualization.

## Declaration of competing interest

The authors declare that they have no known competing financial interests or personal relationships that could have appeared to influence the work reported in this paper.

## Data availability

Data will be made available on request.

## Acknowledgements

The authors thank to the support provided by Research Council of Norway through the HyLINE (294739), M-HEAT (294689) and H2Ninja (309378) projects. A. Díaz gratefully acknowledge funding from projects PID2021-124768OB-C21 and TED2021-130413B–I00. Simulations are carried out on the Betzy high-performance computer clusters at NTNU, Trondheim. Tore Kristiansen is greatly acknowledged for carrying out the in-situ SSRT experiments.

## References

[1] W.H. Johnson, II. On some remarkable changes produced in iron and steel by the action of hydrogen and acids, Proc. Roy. Soc. Lond. 23 (156–163) (1875) 168–179.
[2] G. Domizzi, G. Anteri, J. Ovejero-Garcıa, Influence of sulphur content and inclusion distribution on the hydrogen induced blister cracking in pressure vessel and pipeline steels, Corrosion Sci. 43 (2) (2001) 325–339.
[3] Z. Liu, X. Li, C. Du, L. Lu, Y. Zhang, Y. Cheng, Effect of inclusions on initiation of stress corrosion cracks in X70 pipeline steel in an acidic soil environment, Corrosion Sci. 51 (4) (2009) 895–900.
[4] W.K. Kim, S.U. Koh, B.Y. Yang, K.Y. Kim, Effect of environmental and metallurgical factors on hydrogen induced cracking of HSLA steels, Corrosion Sci. 50 (12) (2008) 3336–3342.
[5] D. Hejazi, A. Haq, N. Yazdipour, D. Dunne, A. Calka, F. Barbaro, E. Pereloma, Effect of manganese content and microstructure on the susceptibility of X70 pipeline steel to hydrogen cracking, Mater. Sci. Eng., A 551 (2012) 40–49.

[6] A. Ikeda, T. Kaneko, F. Terasaki, Influence of Environmental Conditions and Metallurgical Factors on Hydrogen Induced Cracking of Line Pipe Steel vol. 3, 80/8, NACE, Houston, TX. Per copy$, Amagasaki, Japan, Corrosion, 1980. A. Ikeda, T. Kaneko, and F. Terasaki, Sumitomo Metal Industries, Ltd.

[7] J.-Q. Tang, J.-M. Gong, X.-C. Zhang, S.-T. Tu, Comparison on the cracking susceptibility of different low alloy steel weldments exposed to the environment containing wet H2S, Eng. Fail. Anal. 13 (7) (2006) 1057–1064.

[8] Y. Ogawa, M. Hino, M. Nakamura, H. Matsunaga, Pearlite-driven surface-cracking and associated loss of tensile ductility in plain-carbon steels under exposure to high-pressure gaseous hydrogen, Int. J. Hydrogen Energy 46 (9) (2021) 6945–6959.

[9] N. Nanninga, Y. Levy, E.S. Drexler, R. Condon, A. Stevenson, A.J. Slifka, Comparison of hydrogen embrittlement in three pipeline steels in high pressure gaseous hydrogen environments, Corrosion Sci. 59 (2012) 1–9.

[10] T. Zhang, W. Zhao, Q. Deng, W. Jiang, Y. Wang, Y. Wang, W. Jiang, Effect of microstructure inhomogeneity on hydrogen embrittlement susceptibility of X80 welding HAZ under pressurized gaseous hydrogen, Int. J. Hydrogen Energy 42 (39) (2017) 25102–25113.

[11] C. Zhou, B. Ye, Y. Song, T. Cui, P. Xu, L. Zhang, Effects of internal hydrogen and surface-absorbed hydrogen on the hydrogen embrittlement of X80 pipeline steel, Int. J. Hydrogen Energy 44 (40) (2019) 22547–22558.

[12] D. Wang, A.B. Hagen, P. Fathi, M. Lin, R. Johnsen, X. Lu, Investigation of hydrogen embrittlement behavior in X65 pipeline steel under different hydrogen charging conditions, Mater. Sci. Eng., A 860 (2022) 144262.

[13] E.S. Drexler, A.J. Slifka, R.L. Amaro, N. Barbosa, D.S. Lauria, L.E. Hayden, D. G. Stalheim, Fatigue crack growth rates of API X70 pipeline steel in a pressurized hydrogen gas environment, Fatig. Fract. Eng. Mater. Struct. 37 (5) (2014) 517–525.

[14] P. Fassina, F. Brunella, L. Lazzari, G. Re, L. Vergani, A. Sciuccati, Fatigue behavior of pipeline steel under hydrogen environment and low temperature, Procedia Eng. 10 (2011) 3345–3352.

[15] D. Wang, A.B. Hagen, D. Wan, X. Lu, R. Johnsen, Probing hydrogen effect on nanomechanical properties of X65 pipeline steel using in-situ electrochemical nanoindentation, Mater. Sci. Eng., A 824 (2021) 141819.

[16] L. Zhang, W. Cao, K. Lu, Z. Wang, Y. Xing, Y. Du, M. Lu, Effect of the cathodic current density on the sub-surface concentration of hydrogen in X80 pipeline steels under cathodic protection, Int. J. Hydrogen Energy 42 (5) (2017) 3389–3398.

[17] M. Asadipoor, A.P. Anaraki, J. Kadkhodapour, S. Sharifi, A. Barnoush, Macro-and microscale investigations of hydrogen embrittlement in X70 pipeline steel by in-situ and ex-situ hydrogen charging tensile tests and in-situ electrochemical micro-cantilever bending test, Mater. Sci. Eng., A 772 (2020) 138762.

[18] R. Wang, Effects of hydrogen on the fracture toughness of a X70 pipeline steel, Corrosion Sci. 51 (12) (2009) 2803–2810.

[19] E. Koren, C.M.H. Hagen, D. Wang, X. Lu, R. Johnsen, J. Yamabe, Experimental comparison of gaseous and electrochemical hydrogen charging in X65 pipeline steel using the permeation technique, Corrosion Sci. 215 (2023) 111025.

[20] H.K. Birnbaum, P. Sofronis, Hydrogen-enhanced localized plasticity—a mechanism for hydrogen-related fracture, Mater. Sci. Eng., A 176 (1–2) (1994) 191–202.

[21] R.A. Oriani, A mechanistic theory of hydrogen embrittlement of steels, Ber. Bunsen Ges. Phys. Chem. 76 (8) (1972) 848–857.

[22] R. Depraetere, W. De Waele, M. Cauwels, T. Depover, K. Verbeken, M. Boone, S. Hertelé, Influence of stress triaxiality on hydrogen assisted ductile damage in an X70 pipeline steel, Mater. Sci. Eng., A (2022) 144549.

[23] V. Olden, A. Alvaro, O.M. Akselsen, Hydrogen diffusion and hydrogen influenced critical stress intensity in an API X70 pipeline steel welded joint – experiments and FE simulations, Int. J. Hydrogen Energy 37 (15) (2012) 11474–11486.

[24] E. Ohaeri, U. Eduok, J. Szpunar, Hydrogen related degradation in pipeline steel: a review, Int. J. Hydrogen Energy 43 (31) (2018) 14584–14617.

[25] X. Wu, H. Zhang, M. Yang, W. Jia, Y. Qiu, L. Lan, From the perspective of new technology of blending hydrogen into natural gas pipelines transmission: mechanism, experimental study, and suggestions for further work of hydrogen embrittlement in high-strength pipeline steels, Int. J. Hydrogen Energy (2022).

[26] M. Lin, H. Yu, X. Wang, R. Wang, Y. Ding, A. Alvaro, V. Olden, J. He, Z. Zhang, A microstructure informed and mixed-mode cohesive zone approach to simulating hydrogen embrittlement, Int. J. Hydrogen Energy (2022).

[27] L.B. Peral, I. Fernández-Pariente, C. Colombo, Critical hydrogen concentration for crack propagation in a CrMo steel: targeted experiments for accurate numerical modelling, Eng. Fract. Mech. 273 (2022) 108764.

[28] H. Yu, J.S. Olsen, A. Alvaro, L. Qiao, J. He, Z. Zhang, Hydrogen informed Gurson model for hydrogen embrittlement simulation, Eng. Fract. Mech. 217 (2019) 106542.

[29] R. Depraetere, W. De Waele, S. Hertelé, Fully-coupled continuum damage model for simulation of plasticity dominated hydrogen embrittlement mechanisms, Comput. Mater. Sci. 200 (2021).

[30] W. Brocks, R. Falkenberg, I. Scheider, Coupling aspects in the simulation of hydrogen-induced stress-corrosion cracking, Procedia IUTAM 3 (2012) 11–24.

[31] C. Moriconi, G. Hénaff, D. Halm, Cohesive zone modeling of fatigue crack propagation assisted by gaseous hydrogen in metals, Int. J. Fatig. 68 (2014) 56–66.

[32] S. del Busto, C. Betegón, E. Martínez-Pañeda, A cohesive zone framework for environmentally assisted fatigue, Eng. Fract. Mech. 185 (2017) 210–226.

[33] A. Alvaro, V. Olden, O.M. Akselsen, 3D cohesive modelling of hydrogen embrittlement in the heat affected zone of an X70 pipeline steel, Int. J. Hydrogen Energy 38 (18) (2013) 7539–7549.

[34] A. Alvaro, V. Olden, O.M. Akselsen, 3D cohesive modelling of hydrogen embrittlement in the heat affected zone of an X70 pipeline steel – Part II, Int. J. Hydrogen Energy 39 (7) (2014) 3528–3541.

[35] H. Yu, J.S. Olsen, J. He, Z. Zhang, Hydrogen-microvoid interactions at continuum scale, Int. J. Hydrogen Energy 43 (21) (2018) 10104–10128.

[36] D. Ahn, P. Sofronis, R. Doddsjr, On hydrogen-induced plastic flow localization during void growth and coalescence, Int. J. Hydrogen Energy 32 (16) (2007) 3734–3742.

[37] R. Depraetere, W. De Waele, M. Cauwels, T. Depover, K. Verbeken, S. Hertelé, %M doi:10.3390/ma16134839%U, Modeling of Hydrogen-Charged Notched Tensile Tests of an X70 Pipeline Steel with a Hydrogen-Informed Gurson Model 16 (13) (2023) 4839, https://www.mdpi.com/1996-1944/16/13/4839. Materials %@ 1996-1944.

[38] M. Nagumo, K. Takai, The predominant role of strain-induced vacancies in hydrogen embrittlement of steels: overview, Acta Mater. 165 (2019) 722–733.

[39] M.B. Djukic, V. Sijacki Zeravcic, G.M. Bakic, A. Sedmak, B. Rajicic, Hydrogen damage of steels: a case study and hydrogen embrittlement model, Eng. Fail. Anal. 58 (2015) 485–498.

[40] M.B. Djukic, G.M. Bakic, V.S. Zeravcic, A. Sedmak, B. Rajicic, Hydrogen embrittlement of industrial components: prediction, prevention, and models, Corrosion 72 (7) (2016) 943–961.

[41] M. Koyama, C.C. Tasan, E. Akiyama, K. Tsuzaki, D. Raabe, Hydrogen-assisted decohesion and localized plasticity in dual-phase steel, Acta Mater. 70 (2014) 174–187.

[42] A. Nagao, C.D. Smith, M. Dadfarnia, P. Sofronis, I.M. Robertson, The role of hydrogen in hydrogen embrittlement fracture of lath martensitic steel, Acta Mater. 60 (13–14) (2012) 5182–5189.

[43] I.M. Dmytrakh, R.L. Leshchak, A.M. Syrotyuk, Effect of hydrogen concentration on strain behaviour of pipeline steel, Int. J. Hydrogen Energy 40 (10) (2015) 4011–4018.

[44] W. Krieger, S.V. Merzlikin, A. Bashir, A. Szczepaniak, H. Springer, M. Rohwerder, Spatially resolved localization and characterization of trapped hydrogen in zero to three dimensional defects inside ferritic steel, Acta Mater. 144 (2018) 235–244.

[45] Y. Ogawa, D. Birenis, H. Matsunaga, O. Takakuwa, J. Yamabe, Ø. Prytz, A. Thøgersen, The role of intergranular fracture on hydrogen-assisted fatigue crack propagation in pure iron at a low stress intensity range, Mater. Sci. Eng., A 733 (2018) 316–328.

[46] M. Lin, H. Yu, Y. Ding, G. Wang, V. Olden, A. Alvaro, J. He, Z. Zhang, A predictive model unifying hydrogen enhanced plasticity and decohesion, Scripta Mater. 215 (2022).

[47] D. Lopes Pinto, A. El Ouazani Tuhami, N. Osipov, Y. Madi, J. Besson, Simulation of Hydrogen Embrittlement of Steel Using Mixed Nonlocal Finite Elements, European Journal of Mechanics - A/Solids, 2023 105116.

[48] P.W. Bridgman, Studies in Large Plastic Flow and Fracture, Studies in Large Plastic Flow and Fracture, Harvard University Press, 2013.

[49] Z. Zhang, A Complete Gurson Model, Nonlinear Fracture and Damage Mechanics, 2001, pp. 223–248.

[50] V. Tvergaard, A. Needleman, Analysis of the cup-cone fracture in a round tensile bar, Acta Metall. 32 (1) (1984) 157–169.

[51] P.F. Thomason, Three-dimensional models for the plastic limit-loads at incipient failure of the intervoid matrix in ductile porous solids, Acta Metall. 33 (6) (1985) 1079–1085.

[52] Z.L. Zhang, C. Thaulow, J. Ødegård, A complete Gurson model approach for ductile fracture, Eng. Fract. Mech. 67 (2) (2000) 155–168.

[53] M. Lin, H. Yu, Y. Ding, V. Olden, A. Alvaro, J. He, Z. Zhang, Simulation of ductile-to-brittle transition combining complete Gurson model and CZM with application to hydrogen embrittlement, Eng. Fract. Mech. 268 (2022).

[54] H. Gholipour, F.R. Biglari, K. Nikbin, Experimental and numerical investigation of ductile fracture using GTN damage model on in-situ tensile tests, Int. J. Mech. Sci. 164 (2019) 105170.

[55] C.V. Di Leo, L. Anand, Hydrogen in metals: a coupled theory for species diffusion and large elastic–plastic deformations, Int. J. Plast. 43 (2013) 42–69.

[56] A. Díaz, J.M. Alegre, I.I. Cuesta, Coupled hydrogen diffusion simulation using a heat transfer analogy, Int. J. Mech. Sci. 115–116 (2016) 360–369.

[57] R.A. Oriani, The diffusion and trapping of hydrogen in steel, Acta Metall. 18 (1) (1970) 147–157.

[58] A. Díaz, J. Alegre, I.J.I. Cuesta, Coupled hydrogen diffusion simulation using a heat transfer analogy, Int.J. Mech. Sci. 115 (2016) 360–369.

[59] R. Fernández-Sousa, C. Betegón, E. Martínez-Pañeda, Analysis of the influence of microstructural traps on hydrogen assisted fatigue, Acta Mater. 199 (2020) 253–263.

[60] A.J. Kumnick, H.H. Johnson, Deep trapping states for hydrogen in deformed iron, Acta Metall. 28 (1) (1980) 33–39.

[61] H. Huang, W. Shaw, Hydrogen embrittlement interactions in cold-worked steel, Corrosion 51 (1) (1995) 30–36.

[62] A. Zafra, J. Belzunce, C. Rodríguez, Hydrogen diffusion and trapping in 42CrMo4 quenched and tempered steel: influence of quenching temperature and plastic deformation, Mater. Chem. Phys. 255 (2020).

[63] P. Sofronis, Y. Liang, N. Aravas, Hydrogen induced shear localization of the plastic flow in metals and alloys, Eur. J. Mech. Solid. 20 (6) (2001) 857–872.

[64] Y. Wang, X. Wu, Z. Zhou, X. Li, Numerical analysis of hydrogen transport into a steel after shot peening, Results Phys. 11 (2018) 5–16.

[65] H. Husby, M. Iannuzzi, R. Johnsen, M. Kappes, A. Barnoush, Effect of nickel on hydrogen permeation in ferritic/pearlitic low alloy steels, Int. J. Hydrogen Energy 43 (7) (2018) 3845–3861.

[66] Z. Zhang, M. Hauge, J. Ødegård, C. Thaulow, Determining material true stress–strain curve from tensile specimens with rectangular cross-section, Int. J. Solid Struct. 36 (23) (1999) 3497–3516.

[67] D. Hardie, E.A. Charles, A.H. Lopez, Hydrogen embrittlement of high strength pipeline steels, Corrosion Sci. 48 (12) (2006) 4378–4385.
[68] Z.L. Zhang, M. Hauge, C. Thaulow, J. Ødegård, A notched cross weld tensile testing method for determining true stress–strain curves for weldments, Eng. Fract. Mech. 69 (3) (2002) 353–366.
[69] S. Tu, X. Ren, B. Nyhus, O.M. Akselsen, J. He, Z. Zhang, A special notched tensile specimen to determine the flow stress-strain curve of hardening materials without applying the Bridgman correction, Eng. Fract. Mech. 179 (2017) 225–239.
[70] L. Briottet, I. Moro, P. Lemoine, Quantifying the hydrogen embrittlement of pipeline steels for safety considerations, Int. J. Hydrogen Energy 37 (22) (2012) 17616–17623.
[71] M. Wang, E. Akiyama, K. Tsuzaki, Effect of hydrogen and stress concentration on the notch tensile strength of AISI 4135 steel, Mater. Sci. Eng., A 398 (1–2) (2005) 37–46.
[72] A. Shibata, T. Yonemura, Y. Momotani, M.-H. Park, S. Takagi, Y. Madi, J. Besson, N. Tsuji, Effects of local stress, strain, and hydrogen content on hydrogen-related fracture behavior in low-carbon martensitic steel, Acta Mater. 210 (2021) 116828.
[73] R. Walter, W. Chandler, Influence of hydrogen pressure and notch severity on hydrogen-environment embrittlement at ambient temperatures, Mater. Sci. Eng. 8 (2) (1971) 90–97.
[74] T. An, S. Zheng, H. Peng, X. Wen, L. Chen, L. Zhang, Synergistic action of hydrogen and stress concentration on the fatigue properties of X80 pipeline steel, Mater. Sci. Eng., A 700 (2017) 321–330.
[75] M. Wang, E. Akiyama, K. Tsuzaki, Effect of hydrogen on the fracture behavior of high strength steel during slow strain rate test, Corrosion Sci. 49 (11) (2007) 4081–4097.
[76] Z. Xue, J. Faleskog, J.W. Hutchinson, Tension–torsion fracture experiments–Part II: simulations with the extended Gurson model and a ductile fracture criterion based on plastic strain, Int. J. Solid Struct. 50 (25–26) (2013) 4258–4269.
[77] X. Wang, J. Shuai, W. Ren, T. Zhang, J. He, Z. Zhang, A method for determining the ductile damage parameters of high strength steels and weld metal, Adv. Struct. Eng. (2023).
[78] S. Tu, X. Ren, J. He, Z. Zhang, A method for determining material's equivalent stress-strain curve with any axisymmetric notched tensile specimens without Bridgman correction, Int. J. Mech. Sci. 135 (2018) 656–667.
[79] K. Kiuchi, R. McLellan, The solubility and diffusivity of hydrogen in well-annealed and deformed iron, Perspectives in Hydrogen in Metals, Elsevier (1986) 29–52.
[80] H. Yu, J.S. Olsen, A. Alvaro, V. Olden, J. He, Z. Zhang, A uniform hydrogen degradation law for high strength steels, Eng. Fract. Mech. 157 (2016) 56–71.
[81] C. Ayas, V.S. Deshpande, N.A. Fleck, A fracture criterion for the notch strength of high strength steels in the presence of hydrogen, J. Mech. Phys. Solid. 63 (2014) 80–93.